Editors' Suggestion

Nanoscale probing of resonant photonic modes in dielectric nanoparticles with focused electron beams

Qianlang Liu,[1] Steven C. Quillin,[2] David J. Masiello,[2,*] and Peter A. Crozier[1,†]

[1]*School for the Engineering of Matter, Transport and Energy, Arizona State University, 501 E. Tyler Mall, Tempe, Arizona 85287-6106, USA*

[2]*Department of Chemistry, University of Washington, Seattle, Washington 98195-1700, USA*

(Received 16 October 2018; revised manuscript received 17 February 2019; published 3 April 2019)

Understanding the optical responses of nanostructures with high spatial resolution is paramount in photonic engineering. The excitation of resonant optical-frequency geometric modes in oxide nanoparticles is explored using monochromated electron energy-loss spectroscopy in a scanning transmission electron microscope. These geometric or cavity modes are found to produce a progression of resonance peaks within the bandgap regions of the electron energy-loss spectra of CeO_2, TiO_2, and MgO nanoparticles. Complementary simulations of the electron probe combined with analytic Mie analysis are performed to interpret the complex spectral features and to understand their underlying physical origins. The factors that influence the energies, shapes, and strengths of these modes are also investigated and their dependence upon nanoparticle size, geometry, refractive index, aggregation, impact parameter, and electron kinetic energy are elucidated. Taken together, this work demonstrates the unique ability of fast electron spectroscopy to determine the photonic density of states in individual and complex assemblies of dielectric nanoparticles.

DOI: 10.1103/PhysRevB.99.165102

I. INTRODUCTION

Controlling the nanolocalization of light through engineered optical responses in dielectric structures has drawn ever increasing interest due to the importance and variety of applications impacted, ranging from enhanced solar light absorption [1], and ultrasensitive detection of unlabeled molecules [2,3] to highly optimized cavity quantum electrodynamic measurements [4,5]. Owing to their localized surface plasmon responses, noble metal nanostructures have also found great utility in a variety of applications that benefit from capturing and converting incident photons into intense optical near fields, but suffer from losses that inhibit their use in optical communication devices. An alternative approach for optical energy transfer is to employ the photonic modes within the bandgap region of dielectric insulating particles [6]. Here, incident photons with energies less than the bandgap may be trapped as standing waves in the material at specific resonance energies determined by particle size, shape, and refractive index. However, since the photon energy is below the bandgap, losses due to electronic excitation are avoided.

To fully exploit these optical modes for applications, it is necessary to develop a fundamental understanding of the sub-bandgap optical properties of dielectric materials of nanoscale dimension. Characterizing the mode energies, linewidths, and interparticle coupling strengths, as well as their dependences upon nanoparticle morphology and aggregation is critical. It is precisely in this size regime where highly localized measurements that correlate the detailed structure of the observed materials with their optical responses are needed. Electron energy-loss spectroscopy (EELS) coupled to the subnanometer electron probe of a scanning transmission electron microscope (STEM) provides a unique opportunity to measure a material's optical properties with nanometer-scale spatial resolution. The energy-loss spectral intensity can be described by dielectric response theory, and is thus linked to the optical properties of the material [7,8]. The STEM electron beam, which acts as an evanescent source of supercontinuum light, has been employed to determine material optical properties with high spatial resolution [9–12], including the optically bright and dark plasmonic modes in metallic nanostructure [13–17].

Prior work has shown that EELS can also be used to probe cavity modes in semiconductor thin films and nanostructures [18]. Simulated dispersion maps were compared with the experimental spectral peaks observed from nanowires, and understood to arise from waveguide modes induced in the sample by interaction with the fast electron beam [19,20]. These experiments were performed at electron beam energies where the observed modes were significantly influenced by relativistic effects such as Cherenkov radiation. These relativistic effects complicate the interpretation of the energy-loss spectrum and make it more difficult to directly compare effects arising from electron versus photon irradiation. Moreover, in many cases, the modes detected were at energies well above the bandgap where significant photon absorption occur, making them less relevant for light transfer processes.

Recent developments in electron monochromators have now resulted in energy resolutions of ∼10 meV with electron probe sizes of less than 0.2 nm [21–24]. One advantage of using electrons rather than photons to probe resonances in dielectric nanoparticles is that modes of all energies from the bandgap (often in the UV) down to the infrared can be probed simultaneously. As the electron beam is positioned

*Corresponding author: masiello@chem.washington.edu

†Corresponding author: crozier@asu.edu

at different locations surrounding and within the sample, the excitation strength of different modes will be enhanced or diminished, providing information on both the spectral and spatial distribution of target resonances. The spatial variation in the energy-loss spectrum can also be employed to perform a high resolution investigation of the cavity mode hybridization associated with complex geometric arrangements of dielectric nanoparticles. Mapping the modes in two dimensions will allow the relationship between sample geometry, mode energy, and localization to be explored suggesting optimal structures for device applications.

Here we show that STEM EELS performed with an intermediate energy electron beam (40–60 kV) can be employed to explore optical cavity modes with energies lying in the bandgap of dielectric oxide nanoparticles. The lower accelerating voltage minimizes relativistic effects so that the cavity mode peaks observed in the energy-loss spectrum are similar to those measured via optical scattering. Thus, EELS is able to provide detailed information about the energy and linewidth of modes relevant to photonic applications from individual nanoparticles. The particular focus of this work is on investigating the behavior of the geometric resonant optical modes in oxide nanoparticles composed of TiO_2, CeO_2, and MgO using STEM EELS. These particles span a range of bandgaps and refractive indices, and can be synthesized with well-defined shapes to facilitate comparison with modeling. To interpret the spectral features, theoretical models and numerical simulations based on classical electrodynamics are developed and used to interpret the effects of interparticle coupling on the optical properties of hybridized cavity modes in nanoparticle clusters.

II. METHODS

Commercial TiO_2 anatase particles (99.8%) were purchased from Sigma-Aldrich. CeO_2 nanocubes with predominantly (100) surfaces were hydrothermally synthesized following a method described elsewhere [25,26]. The TiO_2 nanoparticles were dispersed onto TEM sample grids (holey carbon film) using a dry preparation method. For CeO_2 nanocubes, in order to maximize the possibility of finding isolated cubes, the powders were first ground and dispersed in deionized water then ultrasonicated for ∼15 min. Dispersion from the top layer of solution was drop cast onto a TEM grid to prepare a sample with isolated CeO_2 cubes.

An aberration-corrected NION UltraSTEM 100 microscope coupled with a monochromator and a Gatan Enfinium spectrometer was employed to acquire all the spectra. The microscope was operated at 60 and 40 kV with an energy dispersion of 5 meV per channel. Full width half maximum of the zero-loss peak was better than 25 meV. Convergence and collection semiangles were 30 and 15 mrad, respectively, with a 1-mm spectrometer entrance aperture. The Gatan Digital Micrograph software was used to process the data. Both EELS line scans and spot acquisitions were performed, where 40–50 s acquisition time was used for each spectrum to improve the signal-to-noise ratio.

Our numerical methods are based upon the coupled-dipole [27] or discrete dipole approximation approach [28], which has been routinely used to model the response of plasmonic nanoparticles to plane wave radiation. As a generalization of these ideas, here we use our previously developed electron-driven discrete dipole approximation [16] to model the STEM electron beam and its interaction with the target specimen. The nanoparticles under study were modeled as perfect cubes, with an interdipole spacing chosen to ensure convergence. The dielectric data for each material was taken from the literature (TiO_2 [29], CeO_2 [30], MgO [31]).

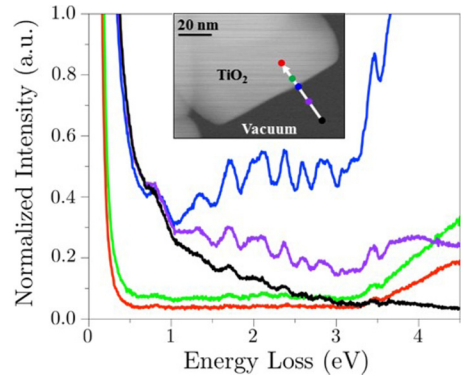

FIG. 1. STEM EELS line scan of an anatase nanoparticle with electron probe moving from vacuum to penetrating configurations as shown in the inset. The STEM acceleration voltage is 60 kV. The impact parameter corresponding to each spectrum is $b = 25$ nm (black); $b = 12$ nm (purple); $b = 0$ (blue); $b = -6$ nm (green); $b = -15$ nm (red). A progression of resonances within the bandgap is clearly visible in the aloof beam configurations.

III. RESULTS AND DISCUSSSION

Figure 1 shows a set of EEL spectra from a STEM line scan across the surface of a 100-nm anatase nanoparticle, revealing a series of pronounced peaks in the bandgap region (bandgap of 3.2 eV) of the spectrum. The anatase nanoparticle is part of a large aggregate of particles and the surface facet is aligned to be parallel to the electron beam and roughly 80 nm in length, as shown in the high-angle annular dark-field (HAADF) image in Fig. 1. In this line scan, the beam begins 25 nm outside of the particle and is scanned to 15 nm inside of the particle. The corresponding spectra can be categorized as either aloof or transmission, depending on whether the beam is located in the vacuum or is penetrating the particle. In the aloof beam geometry, the energy-loss signal is generated as a result of delocalized electron-solid interactions [32]. The influence of the distance from the electron beam to the crystal surface, defined as the impact parameter b ($b > 0$ for aloof and $b < 0$ for transmission geometries), on the aloof spectral intensity has been discussed previously in the literature [24,33].

At 25 nm outside the particle, the spectrum shows a series of small-amplitude resonances in the energy range between 0.5 and 3.5 eV, while the bandgap onset is ∼3.2 eV. As the beam approaches the particle surface, the aloof spectral intensity rises, with the peaks in the bandgap becoming most intense when the electron beam is positioned on the surface. This strong increase in the signal with decreasing impact parameter is expected for the aloof region of the scan [33], however, once the beam enters TiO_2, a pronounced reduction in overall spectral intensity is observed. This overall intensity

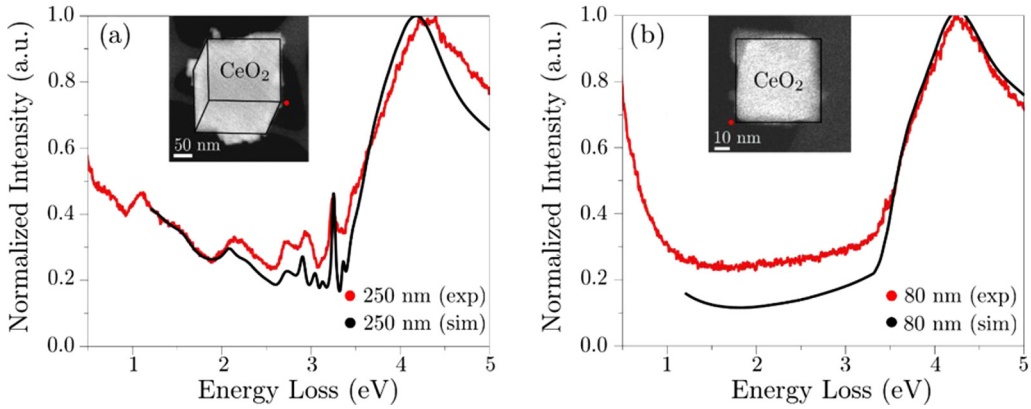

FIG. 2. Experimental (red) and computed (black) aloof beam EEL spectra with the electron beam positioned 4 nm from (a) the corner of a well-defined CeO_2 cube 250 nm in size, and (b) the corner of an 80-nm CeO_2 cube. The incident electron voltage is 60 kV. Simple power-law background intensities are added to both simulations to account for the zero-loss peak tails. The insets are the HAADF images of the 250- and 80-nm cubes with beam positions denoted by the red bullets.

drop in the transmission spectra is mainly because a significant portion of the incident electrons now undergo elastic scattering outside the angle limiting spectrometer entrance aperture resulting in a drop in the signal-to-noise in the bandgap region. In practice, the visibility of the cavity modes is enhanced when the probe is close to the edge of the particle (see Fig. 5) and the aloof beam geometry also enhances the signal-to-noise of the spectral peaks in the bandgap region due to the absence of elastic scattering. Considering the convergent electron probe and the average nanoparticle thickness (∼100–200 nm), the optimum impact parameter to observe the spectral signatures of cavity modes while avoiding elastic scattering contributions is ∼4–5 nm [24].

The behavior of the anatase nanoparticle's bandgap peaks as a function of crystal tilt relative to the electron beam source, as well as the incident electron energy were experimentally explored (see Fig. S1 in Supplemental Material [34]). It was found that crystal tilt leads to no change in the peak energies, and only subtle changes in the peak strengths (Fig. S1a). However, in contrast to crystal orientation, it is evident that the visibility of the bandgap peaks is significantly reduced at lower beam voltage, which corresponds to lower velocity of the fast electron (Fig. S1b). Electrodynamics simulation of the fast electron probe would aid in understanding the origin of these spectral peaks, but the commercial anatase nanoparticles studied here have complicated geometrical shapes and tend to aggregate into irregular clusters. This makes it challenging to determine their precise three-dimensional shape from the projected HAADF images, which is necessary to parametrize the calculation. However, hydrothermally synthesized CeO_2 nanoparticles exhibit a more well-defined near-cubic morphology (Fig. 2), with refractive indices similar to those of TiO_2 [Fig. 4(b)], and are amenable to detailed numerical simulation. Figure 2(a) displays the aloof beam energy-loss spectrum of a 250-nm CeO_2 nanocube (experiment: red, simulation: black), showing peaks in the bandgap region similar to those observed in the TiO_2 particles. This particular nanocube is isolated from other large cubes, although several smaller particles are attached to its surfaces. Due to their small sizes, these particles will not generate spectral peaks in the bandgap as will be discussed, but may affect the appearance of the experimental spectrum as the overall effective shape of the specimen is altered. These complications to the overall particle shape can be approximately accounted for in simulations [16,35] by adjusting the nanocube edge length and tilt. A simple power-law background intensity is also added to the simulation to account for the tail of the zero-loss peak in the experimental spectrum. This yields good agreement between experimental and the simulated aloof EEL spectra. The small discrepancies in the peak energies and strengths between simulation and experiment may be due to inaccuracies in the CeO_2 dielectric data from the literature and an incomplete description of the specimen's morphology. This result shows that the bandgap peaks observed in the spectra can be studied numerically if the specimen geometry and dielectric properties are known.

While possible energy-loss mechanisms are discussed in the Supplemental Material [34], here we focus on gaining a deeper understanding of the physical origin of the bandgap peaks from Mie theory, which provides an analytically exact theory describing the inelastic scattering of photons/electrons by a dielectric sphere. While not identical, the energy transfer mechanism from photon/electron to an oxide nanosphere is qualitatively similar to that of a correspondingly sized oxide nanocube of the same composition, meaning that analytic analysis on the nanosphere should provide an understanding of the spectral features of the nanocube.

The Mie cross section for light scattering by a dielectric sphere of radius r is [36]

$$\sigma_{\mathrm{sca}}(\omega) = \frac{2\pi c^2}{\omega^2} \sum_{l=1}^{\infty} (2l+1)(|a_l|^2 + |b_l|^2), \qquad (1)$$

expressed in terms of the Mie coefficients

$$a_l = \frac{n^2 j_l(nx)[x j_l(x)]' - j_l(x)[nx j_l(nx)]'}{n^2 j_l(nx)\left[x h_l^{(1)}(x)\right]' - h_l^{(1)}(x)[nx j_l(nx)]'}$$

$$b_l = \frac{x j_l(nx) j_l'(x) - nx j_l(x) j_l'(nx)}{x j_l(nx) h_l^{(1)'}(x) - nx h_l^{(1)}(x) j_l'(nx)}$$

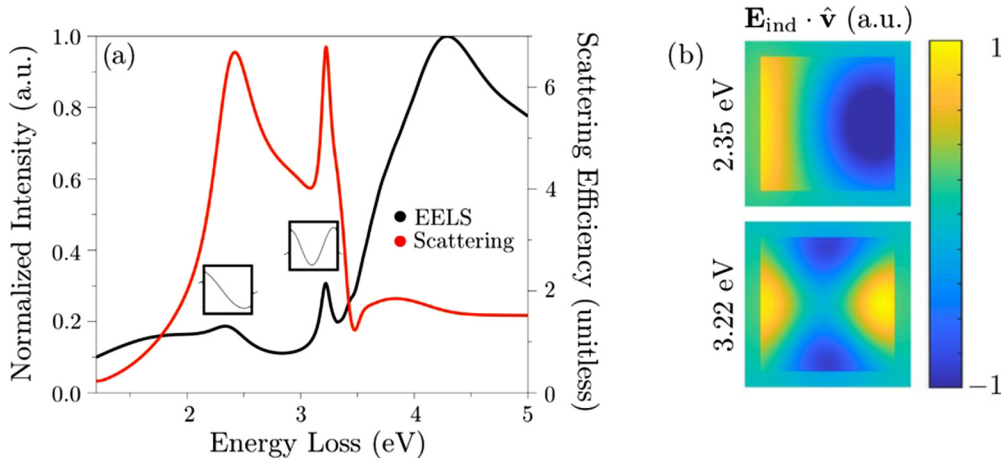

FIG. 3. (a) Simulated aloof EEL (black) and optical scattering (red) spectra of a 160-nm CeO_2 nanocube. The 60-kV electron beam is parallel to the cube surface in the aloof beam geometry, and the polarized plane-wave light field is normal to the cube surface. The two insets display the electric field intensity profiles within the cube at the band-gap resonances. (b) The field maps show the electron-driven electric field distributions associated with the cavity modes at 2.35 eV (top) and 3.22 eV (bottom).

where n is the refractive index and $x = kr = 2\pi r/\lambda = \omega r/c$. It is the denominators of a_l and b_l that encode the resonant frequencies ω of the nanosphere target as zeros. Such poles are parametrically dependent upon both the target index of refraction and the ratio of nanosphere radius r to wavelength λ [e.g., in the dispersive region of the (visible) spectrum for noble metals, it is these poles that encode the spectral locations of the nanosphere's surface plasmon resonances]. However, in the case of Ce, Ti, and Mg oxides, the dielectric function is real-valued and positive and nearly constant below the bandgap. This means that absorption is negligible, and scattering, if finite, is not due to either individual or collective electronic transitions. Analysis of the behavior of the spherical Bessel and Hankel functions j_l and h_l at the roots of the Mie coefficient denominators demonstrates that the spectral peaks within the bandgap region correspond approximately to the situation where an integer multiple of half wavelengths "fit" within the nanosphere. This analytical observation justifies the physical picture of these scattering features as geometric cavity resonances.

Our experimental observations do not involve light scattering but rather inelastic electron scattering via EELS. Fortunately, Mie theory can be applied equally to both optical and electron beam sources [37], and in the case where the sphere's refractive index is real-valued, there is a simple relationship between the two observables. In general, the energy-loss probability per unit of transferred energy is

$$\Gamma^{\text{EELS}}(\omega) = \frac{e^2}{c\hbar^2\omega}\sum_{l=1}^{\infty}\sum_{m=-l}^{l} K_m^2\left(\frac{\omega b}{v\gamma}\right)\left(C_{lm}^{A}\,\text{Im}\,a_l^{\text{EELS}} + C_{lm}^{B}\,\text{Im}\,b_l^{\text{EELS}}\right), \quad (2)$$

where K_m is a modified Bessel function of the second kind, γ is the relativistic Lorentz contraction factor, C_{lm}^{A} and C_{lm}^{B} are velocity dependent but frequency independent coefficients, and $a_l^{\text{EELS}} = ia_l$ and $b_l^{\text{EELS}} = ib_l$ are the EELS Mie coefficients, which are simply connected to those of light scattering. While not obvious, when the refractive index is real-valued, $\text{Im}\,a_l^{\text{EELS}} = |a_l|^2$ and $\text{Im}\,b_l^{\text{EELS}} = |b_l|^2$, meaning that both $\Gamma^{\text{EELS}}(\omega)$ and $\sigma_{\text{sca}}(\omega)$ have the same pole structure. This makes explicit the fact that EELS is a local measure of extinction, with extinction being equivalent to scattering since absorption is zero in this case.

Figure 3 shows the correlation between the computed induced electric field distribution in a 160 nm CeO_2 particle and the bandgap peaks in the energy-loss and optical scattering spectra. The electric field distributions are consistent with standing electromagnetic waves of different wavelengths confined within the nanoparticle. The low energy peak at 2.35 eV corresponds to a wavelength of roughly double the particle size, and the 3.22-eV peak corresponds to a wavelength of roughly the same size as the particle. Taken together, this analysis shows that the EELS bandgap peaks are precisely those same geometric cavity modes emerging in light scattering.

Figure 4(a) compares the simulated EEL spectra of individual TiO_2 and CeO_2 nanocubes, both 160 nm in size (the smaller particle size simplifies the spectrum by reducing the number of peaks in the bandgap). In both spectra, the electron beam is positioned at a low symmetry point outside of the particle with a 4-nm impact parameter [indicated in Fig. 4(a), inset]. The simulated spectral features below 3.5 eV from TiO_2 and CeO_2 are quite similar, except for a small blue shift in the peak positions in the CeO_2 spectrum. The similarity of the spectra correlates with the similarity in the energy-dependent refractive indices of CeO_2 and TiO_2 [Fig. 4(b)]. This implies that the optical responses in the bandgap region of these two materials will be very similar if their geometrical shapes are the same.

The effect of changes in refractive index on cavity modes can be made by examining the computed aloof spectrum of MgO, which has a much smaller refractive index than titania and ceria [see Fig. 4(a)]. All spectra are normalized so that the spectral intensities are approximately equal above the bandgap. In the MgO spectrum, a gentler intensity variation in the bandgap region (<7.3 eV) is displayed. This behavior is expected based on Mie analysis, where the geometric resonance conditions in similarly sized nanoparticles composed

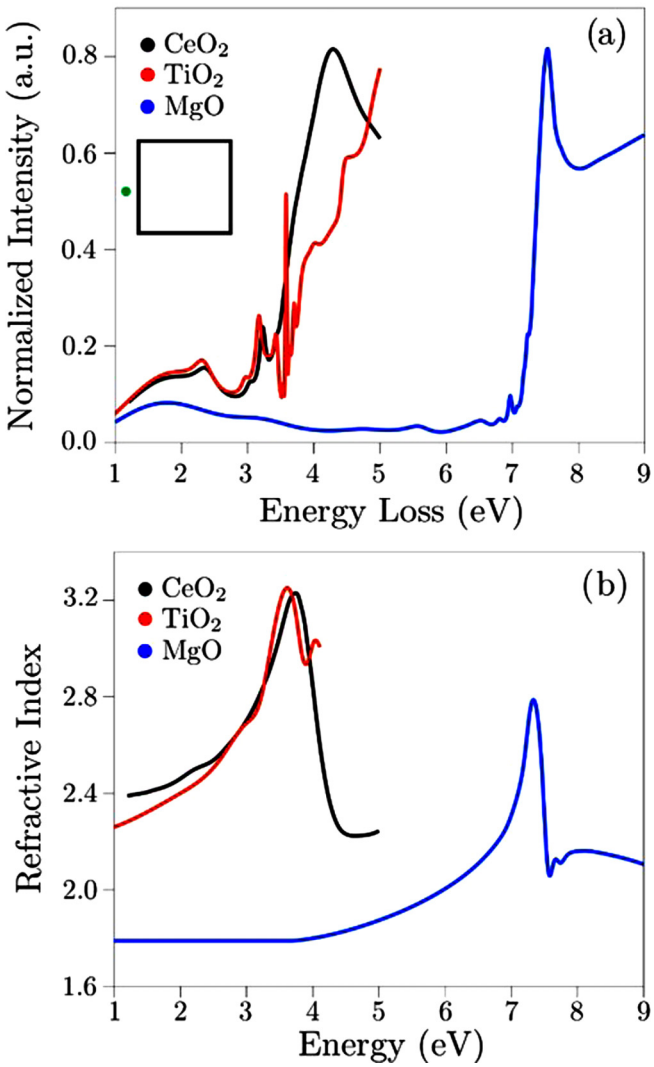

FIG. 4. (a) Calculated aloof EEL spectra of TiO_2, CeO_2 and MgO cubes with the same edge length (160 nm). In each spectrum, the 60-kV electron beam is positioned at $b = 4$ nm outside of the nanoparticle surface at a low symmetry point. (b) The real-valued component of the energy dependent refractive indices of the three materials.

of materials of low refractive index are only satisfied at energy losses just below the band edge. This agrees with our experimental observation from MgO where sharp EELS peaks within the bandgap region are not observed [24].

In addition, Fig. 5 shows the simulated spectrum of a 160-nm CeO_2 nanocube's cavity mode resonances as a function of electron beam position, demonstrating that cavity modes are best excited in the aloof beam configuration ($b = +4$ nm from the cube surface, black). Conversely, excitation of CeO_2 electrons from the valence to conduction band is most efficient when the electron beam is positioned to penetrate the nanocube as evidenced by the larger spectral intensities after the bandgap onset ($b = -4$ nm from the cube surface, red; $b = -69$ nm from the cube surface, blue). Variation of the CeO_2 nanocube size ($l = 80$ nm and 160 nm) and electron beam acceleration voltage are also explored (see Fig. S2 in the Supplemental Material [34]). Consistent

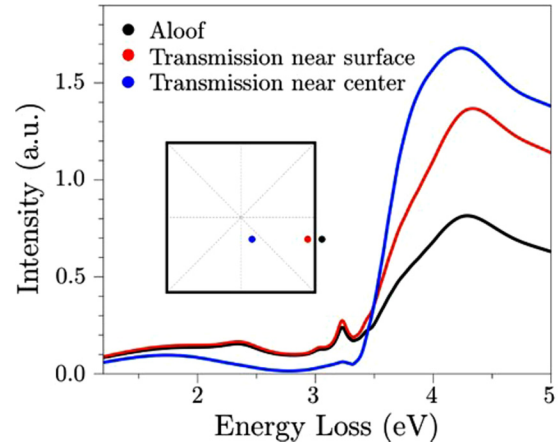

FIG. 5. Calculated EEL spectra from three beam positions for a 160-nm CeO_2 cube with 60-kV incident electrons. The inset displays the 2D projection of the cube with the three low symmetry beam positions (colored bullets) when looking down the beam direction. Dashed lines represent the mirror planes of the cube.

with experiment [Fig. 2(b)], the 80-nm nanocube does not support cavity mode resonances within the bandgap for any of the accelerating voltages considered, while the 160-nm nanocube shows an increasing probability for excitation of cavity modes with increasing acceleration voltage (i.e., electron kinetic energy). It is worth commenting on the effect of these cavity modes on the ability to make accurate measurements of bandgaps as discussed in the literature [38–40]. The importance of suppressing Cerenkov contributions by either working at lower accelerating voltages or collecting the spectral information at higher scattering angles is now recognized. For measurements of bandgaps from nanoparticles, selecting particles that are small and avoiding particle aggregates will help with accurate bandgap determinations. Another point worth mentioning is the degree to which these photonic modes will show up in the spectrum from a thin film sample which is not tilted. The limited sample thickness may lead to geometric resonances along the beam propagation direction. For the refractive indices of interest here, the sample would need to be 150 nm or greater to see modes similar to those observed in the nanoparticles. For the accelerating voltages employed here (40 and 60 kV), the spectral attenuation due to elastic scattering will be very large causing a significant drop in the spectral intensity. In addition, in electron scattering, the momentum transfer is predominantly normal to the incident beam so the probability of exciting modes along the beam direction will be small. Thus, while photonic modes may be present in uniform films, the signal-to-noise of the spectral features induced by these modes may be small.

The hybridization of geometric resonances in photonic crystals [41,42] and chains of dielectric particles [6] has been measured using a variety of optical characterization techniques. Here we explore the effect of coupling between neighboring oxide nanoparticles in spectroscopy through simulation. Figure 6(a) compares the energy-loss spectrum of a CeO_2 nanocube dimer (red) to that of a monomer (black). A pronounced splitting of the monomer cavity resonance near 3.2 eV is observed in the dimer spectrum, indicative

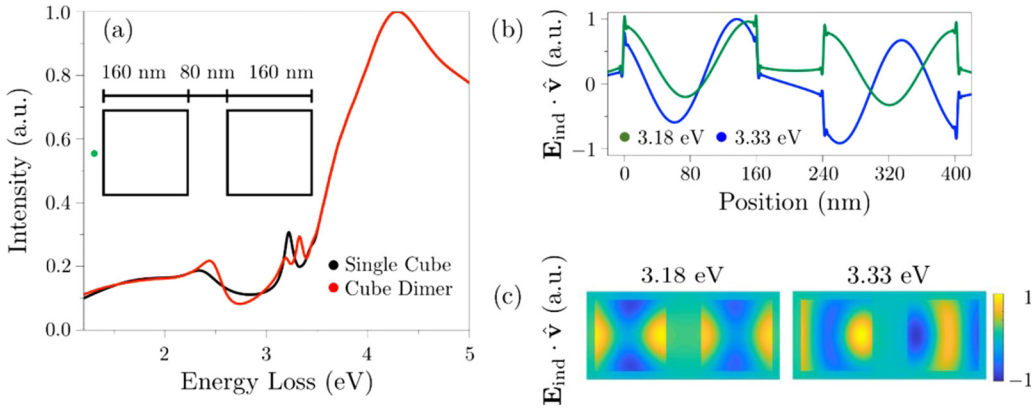

FIG. 6. (a) Calculated aloof EEL spectra of a CeO_2 nanocube dimer (red) and monomer (black) showing the signature of cavity mode hybridization in the splitting of resonance peaks around 3.2 eV. The edge length of each nanocube is 160 nm, and the dimer geometry is displayed in the inset. Panels (b), (c) display the projected electric field profiles of the hybridized cavity modes observed in the spectrum in panel (a). The lower and higher energy modes correspond to the in-phase and out-of-phase hybridized geometric resonances of the dimer.

of hybridization into symmetric and antisymmetric standing waves spanning the dimer cavity. The one-dimensional (1D) and 2D spatial dependences of the lower and higher energy cavity modes are illustrated in panels (b) and (c) of Fig. 6. In both cases the component of the induced electric cavity resonance along the electron beam trajectory ($\hat{\boldsymbol{v}}$) is plotted, clearly demonstrating cavity mode hybridization. Such understanding is useful in the interpretation of small nanoparticle aggregates such as in our original investigations of anatase nanoparticles. These hybrid modes from complex nanostructures can be experimentally mapped pointing the way forward to develop optimal geometries for device applications.

IV. CONCLUSION

We have observed resonant photonic modes in individual and few-particle assemblies of MgO, TiO_2, and CeO_2 nanoparticles using a nanometer dimension electron beam in a monochromated STEM. The modes appear in the EEL signal as a progression of spectral peaks within the bandgap region (where energy absorption is negligible) from relatively large nanoparticles. Electrodynamics simulations combined with analytic Mie analysis of the electron probe facilitate the interpretation and understanding of the physical origin of these spectral features. The peaks result from the excitations of geometric resonance modes, or cavity modes, in the dielectric particles and are most clearly visible when the fast electron beam is near the particle surface even in the aloof geometry where the beam is positioned a few nanometers outside the sample. This resonance behavior is found to be encoded in the scattering properties of the oxide particles when exposed to either electrons or light. The energies and shapes of the cavity modes are determined by the size, geometry, and refractive index of the oxide. Oxides with relatively small refractive index or small particle size (<100 nm) show no obvious cavity mode excitation. The strength of the coupling between the different cavity modes and the fast electron beam is determined by the probe position. The exploration of hybridized cavity modes in oxide nanoparticle dimers is also demonstrated. This work shows the unique ability of STEM EELS to probe the local photonic density of states in individual and ensembles of dielectric nanoparticles. Monochromated STEM EELS particularly, in the aloof geometry, provides an approach to characterize the localization of optical responses in complex dielectric nanostructures.

ACKNOWLEDGMENTS

We acknowledge the use of NION UltraSTEM at John M. Cowley Center for High Resolution Microscopy at Arizona State University. Financial support from US Department of Energy under Award No. DE-SC0004954 (P.A.C.), the DOE Basic Energy Sciences under Award No. DE-SC0018040 (D.J.M.), and the National Science Foundation (NSF) under Award No. CHE-1664684 (D.J.M.) is gratefully acknowledged.

[1] S. Nishimura, N. Abrams, B. A. Lewis, L. I. Halaoui, T. E. Mallouk, K. D. Benkstein, J. van de Lagemaat, and A. J. Frank, J. Am. Chem. Soc. **125**, 6306 (2003).
[2] F. Vollmer, D. Braun, A. Libchaber, M. Khoshsima, I. Teraoka, and S. Arnold, Appl. Phys. Lett. **80**, 4057 (2002).
[3] M. A. Santiago-Cordoba, S. V. Boriskina, F. Vollmer, and M. C. Demirel, Appl. Phys. Lett. **99**, 073701 (2011).
[4] K. J. Vahala, Nature (London) **424**, 839 (2003).
[5] R. Miller, T. E. Northup, K. M. Birnbaum, A. Boca, A. D. Boozer, and H. J. Kimble, J. Phys. B: At. Mol. Opt. Phys. **38**, S551 (2005).
[6] G. S. Blaustein, M. I. Gozman, O. Samoylova, I. Y. Polishchuk, and A. L. Burin, Opt. Express **15**, 17380 (2007).
[7] J. Hubbard, Proc. Phys. Soc. Sect. A **68**, 976 (1955).

[8] R. H. Ritchie, Phys. Rev. **106**, 874 (1957).
[9] D. T. L. Alexander, P. A. Crozier, and J. R. Anderson, Science **321**, 833 (2008).
[10] F. J. García de Abajo, Rev. Mod. Phys. **82**, 209 (2010).
[11] J. Zhu, P. A. Crozier, P. Ercius, and J. R. Anderson, Microsc. Microanal. **20**, 748 (2014).
[12] F. J. García de Abajo and M. Kociak, Phys. Rev. Lett. **100**, 106804 (2008).
[13] M. Bosman, V. J. Keast, M. Watanabe, A. I. Maaroof, and M. B. Cortie, Nanotechnology **18**, 165505 (2007).
[14] J. Nelayah, M. Kociak, O. Stéphan, F. J. García de Abajo, M. Tencé, L. Henrard, D. Taverna, I. Pastoriza-Santos, L. M. Liz-Marzán, and C. Colliex, Nat. Phys. **3**, 348 (2007).
[15] I. Alber, W. Sigle, F. Demming-Janssen, R. Neumann, C. Trautmann, P. A. van Aken, and M. E. Toimil-Molares, ACS Nano **6**, 9711 (2012).
[16] N. W. Bigelow, A. Vaschillo, V. Iberi, J. P. Camden, and D. J. Masiello, ACS Nano **6**, 7497 (2012).
[17] D. Rossouw and G. A. Botton, Phys. Rev. Lett. **110**, 066801 (2013).
[18] A. Yurtsever, M. Couillard, and D. A. Muller, Phys. Rev. Lett. **100**, 217402 (2008).
[19] I. Arslan, J. K. Hyun, R. Erni, M. N. Fairchild, S. D. Hersee, and D. A. Muller, Nano Lett. **9**, 4073 (2009).
[20] J. K. Hyun, M. P. Levendorf, M. Blood-Forsythe, J. Park, and D. A. Muller, Phys. Rev. B **81**, 165403 (2010).
[21] O. L. Krivanek, T. C. Lovejoy, N. Dellby, T. Aoki, R. W. Carpenter, P. Rez, E. Soignard, J. Zhu, P. E. Batson, M. J. Lagos, R. F. Egerton, and P. A. Crozier, Nature (London) **514**, 209 (2014).
[22] W. J. Bowman, K. March, C. A. Hernandez, and P. A. Crozier, Ultramicroscopy **167**, 5 (2016).
[23] P. A. Crozier, T. Aoki, and Q. Liu, Ultramicroscopy **169**, 30 (2016).
[24] Q. Liu, K. March, and P. A. Crozier, Ultramicroscopy **178**, 2 (2017).
[25] Z. Yang, K. Zhou, X. Liu, Q. Tian, D. Lu, and S. Yang, Nanotechnology **18**, 185606 (2007).
[26] Z. Yang, Y. Yang, H. Liang, and L. Liu, Mater. Lett. **63**, 1774 (2009).
[27] E. M. Purcell and C. R. Pennypacker, Astrophys. J. **186**, 705 (1973).
[28] B. T. Draine and P. J. Flatau, J. Opt. Soc. Am. A **11**, 1491 (1994).
[29] M. Landmann, E. Rauls, and W. G. Schmidt, J. Phys.: Condens. Matter **24**, 195503 (2012).
[30] K. Järrendahl and H. Arwin, Thin Solid Films **313–314**, 114 (1998).
[31] D. M. Roessler and W. C. Walker, Phys. Rev. **159**, 733 (1967).
[32] P. A. Crozier, Ultramicroscopy **180**, 104 (2017).
[33] A. Howie and R. H. Milne, Ultramicroscopy **18**, 427 (1985).
[34] See Supplemental Material at http://link.aps.org/supplemental/10.1103/PhysRevB.99.165102 for discussion of the energy-loss mechanisms as well as data showing cavity modes dependence on crystal tilt, incident electron energy, and CeO2 particle size.
[35] N. W. Bigelow, A. Vaschillo, J. P. Camden, and D. J. Masiello, ACS Nano **7**, 4511 (2013).
[36] C. F. Bohren and D. R. Huffman, *Absorption and Scattering of Light by Small Particles* (Wiley, New York, 2008).
[37] F. J. García de Abajo, Phys. Rev. B **59**, 3095 (1999).
[38] R. Erni, Ultramicroscopy **160**, 80 (2016).
[39] S. Korneychuk, B. Partoens, G. Guzzinati, R. Ramaneti, J. Derluyn, K. Haenen, and J. Verbeeck, Ultramicroscopy **189**, 76 (2018).
[40] M. Stöger-Pollach, Micron **39**, 1092 (2008).
[41] A. Majumdar, A. Rundquist, M. Bajcsy, V. D. Dasika, S. R. Bank, and J. Vučković, Phys. Rev. B **86**, 195312 (2012).
[42] A. Majumdar, A. Rundquist, M. Bajcsy, and J. Vučković, Phys. Rev. B **86**, 045315 (2012).